Numerical modelling of the evolution of the boundary layer during a radiation fog event.

D. K. E. Smith[1], I. A. Renfrew[1], J. D. Price[2], S. R. Dorling[1]

1 - Centre for Ocean and Atmospheric Sciences, School of Environmental Sciences, University of East Anglia, Norwich Research Park, Norwich, NR4 7PW, UK

2 - Met Office Research Unit, Cardington Airfield, Shortstown, Bedfordshire, UK

Abstract

Despite the impact it has on human activity, particularly transport, accurate forecasting of fog remains a major challenge for numerical weather prediction models. The complex interaction between various physical processes many of which are parametrised and highly sensitive to small changes is one of the key reasons for poor fog forecasts. One challenge for numerical models is predicting the structure of the boundary layer, which often undergoes a transition from statically stable to weakly unstable during the life cycle of a fog event. The recent local and non-local fog experiment (LANFEX) has provided a new comprehensive and detailed observational data set of fog events. Here a case study has been used as a basis to investigate the impact of the humidity of the residual layer and wind speed on the stability of the boundary layer during a fog event. We find a very high sensitivity in the timing of the stability transition during the fog event; for example, a +3% relative humidity perturbation results in a delay of almost 3 hours, while a 0.45ms^{-1} 10m wind speed perturbation results in a delay of more than 8 hours.

Introduction

The impact of fog is often understated; however, the reduction in visibility caused by fog leads to huge disruptions for air, sea and land transport which causes financial and human losses comparable to losses from tornadoes or severe tropical storms (Gultepe et al., 2007). The accurate forecasting of fog is essential to reduce these disruptions; indeed this need is becoming ever greater as dependencies on transport, particularly aviation, increase. Although there is an abundance of studies on fog, it is still a phenomenon which is not fully understood due to the complex interaction between a myriad of physical processes and its variability in time and space.

Different types of fog are commonly categorised by the mechanism responsible for its formation. The focus of this is study is radiation fog where radiative cooling is the primary mechanism for its formation. Figure 1 is a schematic of the life-cycle of a typical radiation fog. Prior to fog formation,

under clear skies, the temperature evolution is dominated by radiative cooling and an inversion forms near the surface after sunset. The inversion slowly deepens as radiative cooling continues and the static stability suppresses turbulence. This provides the conditions necessary for radiation fog to form. The role of turbulence on fog formation is often contradictory, for example, Roach and Brown (1976) propose that a virtual cessation of turbulence occurs allowing radiative cooling to result in the formation of fog while, alternatively, Rodhe (1962) and Duynkerke (1999) propose that turbulent mixing of near saturated eddies of different temperatures result in saturation and the formation of fog.

After initial formation, the fog can deepen, initially within the surface inversion. This stage of the fog life-cycle will be referred to as shallow stable radiation fog (see figure 1b). As this shallow stable radiation fog develops, it eventually becomes optically thick fog, usually defined as being opaque to thermal radiation (in the 8-12 micron range) and may be detected at the surface by an increase in downwelling longwave radiation. After a fog becomes optically thick the fog top becomes the primary location of radiative cooling. Consequent fog top cooling, which produces negatively buoyant air at the fog top that sinks and eventually reaches the surface, combined with a halt in surface cooling erodes the stability of the boundary layer evolving it to a saturated adiabatic temperature profile. A fog which has undergone this transition in boundary layer stability is referred to as a deep adiabatic radiation fog (see figure 1c). The transition from a shallow stable radiation fog to a deep adiabatic radiation fog takes on average 2 hours from when the fog becomes optically thick and it has been found to occur in approximately 50% of radiation fog cases in central England (Price 2011). Deep adiabatic radiation fogs tend to be longer lived and can persist throughout the day unlike shallow stable radiation fogs which tend to dissipate after sunrise (Price 2011). In addition to the lifespan difference between shallow and deep fog, another important reason to understand the deepening process is that many boundary layer parametrisation schemes, such as that of Lock et al. (2000), rely on the model producing the correct boundary layer types in order to calculate the turbulent transport of heat and moisture. This highlights the importance that understanding and accurately simulating the evolution of the boundary layer has on accurate forecasts of fog.

The aim of this study is to investigate the impact that both wind speed and humidity of the residual layer, the portion of the nocturnal atmospheric boundary layer which is well mixed and above the surface inversion (Labelled in figure 1), have on the timing of the evolution and eventual dissipation of radiation fog. However, there are also other factors which are important such as aerosol-fog interactions (Boutle et al. 2017) and advection (Porson et al. 2011 and Guedalia and Bergot (1994)) but investigating these processes is beyond the scope of this article.

Method

To investigate the impact that the wind speed and humidity of the residual layer have on the development of fog we carry out experiments using a single-column atmospheric model. Single-column models have the benefit of being computationally cheap, containing the equivalent of a single grid point from a 3D model and are easier to focus on particular questions through controlling their large scale forcing.

The single-column version of the Met Office's Unified Model (MetUM) has been used for these experiments and will hereafter be referred to as the SCM. It has been configured with 140 vertical levels with 18 below 250m and the first model level at 1m for wind and 2m for temperature and humidity. The MetUM contains various physical parametrisations for sub-grid scale processes: including radiation (Edwards and Slingo, 1996), vertical mixing in the boundary layer (Lock et al., 2000), a large-scale cloud parametrisation (Smith, 1990), and a cloud microphysics parametrisation (Wilson and Ballard, 1999) which incorporates the updated cloud droplet number profile discussed by Boutle et al. (2017). The MetUM is coupled to the Joint UK Land Environment Simulator (JULES, Best et al., 2011). JULES contains information about the properties of the land surface including soil moisture and temperature, albedo and surface roughness. Fog can be diagnosed using the model's visibility scheme, which uses a single monodisperse dry aerosol concentration that is hydrated using a Köhler curve (Clark et al., 2008). Given significant moisture, the scheme forms fog with the size and number of particles used to calculate an extinction coefficient which is then used in Koschmieder's Law (Koschmieder, 1924) to calculate visibility.

A case from the recent LANFEX (the local and non-local fog experiment, Price et al., 2018) field campaign was selected as a basis for the SCM experiments. The case chosen was the first intensive observation period of LANFEX (IOP1) which was based at the Met Office research unit site at Cardington, Bedfordshire, UK. IOP1 was a case of prolonged shallow stable radiation fog which formed at 1745 UTC 24 November 2014. It remained a shallow stable radiation fog for 10 hours and only became a deep adiabatic radiation fog an hour before dissipation at 0815 UTC 25 November 2014. This case is ideal for simulating using a SCM as there was no significant advection and the synoptic conditions remained approximately stationary over the night of the case study. Figure 2 shows the surface analysis chart at 1800 UTC 24 November 2014 shortly after the fog was observed at Cardington. Overnight on the 23 November 2014 an area of high pressure developed over the UK. This remained the situation throughout the 24 November 2014 which provided ideal conditions for fog to form. This area of high pressure moved on the 25 November 2014 with higher winds and cloud cover preventing the reformation of fog during the following night.

A wide array of measurements were taken during IOP1 and in depth details are presented in Price et al. (2018). Instruments included a cloud droplet probe and turbulence probe flown from a tethered balloon, a 50m tower which houses instruments that take high frequency measurements of temperature, humidity and wind, surface radiation instruments, sub-surface instruments and radiosondes.

The SCM was initialised, prior to fog formation, with radiosonde data from a launch at 1700 UTC 24 November 2014, and with observed soil properties. The initial winds have an approximate log-profile with winds of 1.15ms^{-1} at 10m, 2.25ms^{-1} at 100m and approximately 4ms^{-1} in the boundary layer above 200m. Note the SCM was run with a wind relaxation forcing which relaxed the model winds towards the observed winds from the five subsequent radiosonde launches during the night. The 10m wind remained below 1.75ms^{-1} overnight. This setup formed the control simulation of the SCM.

Two sets of sensitivity experiments are examined – perturbing the wind and the humidity of the residual layer. To perform the wind perturbation experiments the initial winds and wind forcing were perturbed by 1ms^{-1}, 2ms^{-1} and 3 ms^{-1} at 100m and above (with a linear interpolation of the perturbation to zero at the surface which results in a ~0.15ms^{-1}, ~0.3ms^{-1} and ~0.45ms^{-1} perturbation respectively at 10m). The wind perturbations were selected to be within the observed range of variability at Cardington. The aim of these experiments was to assess the impact wind speed and wind shear changes have on the development of fogs and the consequent timing of the stability transition, rather than find a critical speed at which fog will not form. Therefore, the maximum perturbation was restricted to 3ms^{-1}.

The humidity perturbation experiments were performed by perturbing the relative humidity by ± 3% above the stable surface layer at 42m at 1700 UTC. This falls within the 2-5% RH uncertainty of the radiosonde relative humidity measurements during the LANFEX campaign (Price et al., 2018). Finally a combination of both the humidity and wind perturbations were performed to assess the interaction between the two.

Results

Figure 3 shows the temporal evolution of the simulated liquid water content and the observed fog top height derived from a cloud droplet probe attached to a tethered balloon which was used to conduct profiles during IOP1. The control simulation produces fog from 1750 UTC. The fog develops vertically within a stable boundary layer until 2130 UTC, when a thin mixed layer at the base of the fog forms. By 2220 UTC the fog in the control simulation is of a similar depth to the observed fog, 42m compared to the observed 50m. However, the observed fog is within a stable boundary layer

without the thin mixed layer at its base. The fog continues to develop in the control simulation and by 0330 UTC the fog is 100m deep, an over-estimate compared to observations. The control simulation continues to overestimate fog depth until the final observed liquid water profile at 0750 UTC. The observed fog appears to lift into stratus cloud from 0815 UTC on the 25 November 2014 whereas the control simulation produces fog which persists throughout the day. The over production of fog here is consistent with other cases for which the SCM has been run and is the focus of continuing work.

Table 1 shows the formation time, when the 1.5m visibility drops below 1km, the timing of the stability transition, when the boundary layer first becomes unstable and the dissipation time, when the 1.5m visibility returns to being above 1km, for the wind perturbation experiments and observations. The perturbations have no impact on the formation time as this only occurs 50 minutes after the model is initialised and this is not enough time for the perturbations to have a significant impact on the boundary layer temperature and humidity. However, they make a significant difference to the time the boundary layer becomes unstable; 2130 UTC in the control simulation compared to 0545 UTC in the $3ms^{-1}$ wind speed experiment (with this transition occurring at 2300 UTC and 0200 UTC in the $1ms^{-1}$ and $2ms^{-1}$ perturbation respectively). This result is the converse of that in clear stable boundary layers where the stability of the boundary layer erodes in higher winds. Also, in the highest wind speed case the fog dissipates at 1100 UTC compared to the persistent fog in the control simulation.

The mechanism responsible for the difference in the stability transition is investigated further here for the SCM simulations. Figure 4 shows the difference in the evolution of the lowest 250m of the atmosphere between the wind perturbation experiments. At 1800 UTC, only 1 hour after initialisation, all the simulations have a fog layer with a depth of 10m and a maximum liquid water content of 0.075 gkg^{-1}, large enough for the diagnosed visibility to be less than 1km. There is greater specific humidity above the fog layer than in it, indicating that cooling is responsible for its formation rather than any changes in specific humidity. There is a significant difference in the profile of total water content between the experiments, but little difference in the temperature profile. The total specific humidity difference is due to higher wind shear in the higher wind speed experiments, leading to a greater turbulent kinetic energy and greater turbulent moisture flux transport (figure 5). The greater vertical mixing (with the perturbed winds) increases the moisture flux divergence in the lowest 100m, resulting in a turbulent transport of moisture out of this layer, hence drying it. The impact of this specific humidity difference on the fog layer can be seen in the 2100 UTC profiles with the control experiment producing a fog layer of approximately 50m whereas the $+3ms^{-1}$ run has a shallower fog of about 30m. By 0000 UTC the influence the fog has on boundary layer stability is

becoming more evident with the boundary layer in the control (and the +1ms^{-1}) runs becoming unstable near the surface. By 0300 UTC this difference is clear in all 4 simulations with the control simulation having a deeper unstable boundary layer with a fog depth just below 100m whereas the highest wind speed case has a fog layer of 25m within a stable boundary layer. Note the increase in negative moisture flux at the lowest model level in the higher wind speed runs indicates an increase in dew formation and greater moisture removed from the atmosphere (figure 5).

After sunrise all 4 simulations produce rather similar fog layers (i.e. liquid water contents) but with very different total specific humidity and potential temperature structures (figure 6). The control simulation has the coolest boundary layer, approximately 271K, and the lowest total specific humidity, approximately 3.7 gkg^{-1} at 1000 UTC. The boundary layer structure differences are created by the differing wind forcings and consequent fog developments. In the morning the highest wind forcing run has a larger relative humidity above the fog layer as it is cooler and contains more moisture (a higher specific humidity) which enhances growth. The warmer boundary layer in the +3ms^{-1} simulation results in the earlier dissipation of the fog, albeit in a very thin layer near the surface at 1200 UTC although this is enough to increase the surface visibility to over 1km.

The results from the humidity perturbation experiments are summarised in table 2. Like the wind perturbation experiments there is no difference in the fog formation time. The residual layer humidity does have an impact on the stability transition. An hour and half difference between the -3% RH perturbation and +3% perturbation with the transition occurring at 2230 UTC and 2100 UTC respectively. All three simulations maintain the fog during the day on the 25 November 2014.

Figure 7 shows the difference in the evolution of the lowest 250m of the atmosphere between the humidity perturbation experiments. There is no difference in the fog depth and liquid water content until the fog reaches the height of the relative humidity perturbation (42m). After the fog reaches this height it develops more rapidly as there is more moisture available, so by 2100 UTC the +3% perturbation is deeper with a greater liquid water content (as less fog top cooling is necessary for saturation to be reached). The difference in the fog structure also impacts the temperature causing a deeper stable layer with higher near surface temperatures in the +3% perturbation run. By midnight the fog in the -3% run has a lower liquid water content than the control and a shallower unstable layer. By 0300 UTC the +3% perturbation has the deepest unstable layer and the -3% perturbation the shallowest.

The fog depth, liquid water content and specific humidity profiles below 42m are the same in the simulations prior to the fog reaching the height of the perturbations which indicates there has been

little to no mixing between the residual layer and the stable surface layer prior to the fog developing above 42m. The very small TKE in these simulations restricts moisture transport.

To examine humidity sensitivity with slightly stronger wind forcing, the humidity perturbation experiments were re-run with the highest wind forcing, the +3ms^{-1} run, to investigate the impact the humidity of the residual layer has on the timing of the stability transition in more turbulent conditions.

Table 3 summaries the formation, stability transition and dissipation times of the humidity perturbation with the +3ms^{-1} wind forcing experiments. The relative humidity perturbation with the greater wind forcing has a greater impact on the timing of the stability transition than in the control wind case; the difference in the timing of the transition between the -3% and +3% relative humidity runs is now 5 hours, compared to just 1.5 hours with the control wind forcing. However, note in the -3% run the stability transition occurs after sunrise and therefore the transition is influenced by the insolation. The difference between the dissipation times is less than the difference in the stability transition, a 2 hour difference between the -3% and +3% (with +3ms^{-1} wind forcing) runs.

Including the +3ms^{-1} wind forcing produces fog of different depths before the fog reaches the height of the perturbation (figure 8). At 0300 UTC all 3 simulation are producing shallow stable fog with the +3% RH perturbation simulation producing a slightly thicker deeper fog. By 0700 UTC the difference in the fog depth between the 3 simulations is greater with the +3% simulation three times as deep with a peak liquid water content of 0.288 gkg^{-1} compare to the -3% simulation which has a peak liquid water content of 0.085 gkg^{-1}.

The dissipation in all three runs occurs with the fog layer lifting into stratus cloud, which can be seen in the -3% run at 1000 UTC and occurs later in the other simulations. The fog top continues to develop in the morning from continued radiative cooling and entrainment. The thinner fog in the -3% simulation allows more solar radiation to reach the surface and, despite a lower incoming longwave radiation from the thinner fog, the net radiation is greater at the surface, leading to a warmer surface. This increased warming combined with the slightly lower specific humidity in the boundary layer (from the entrainment of the dryer air caused by the perturbation), results in an earlier dissipation in the -3% RH run.

The difference between the simulations with higher wind forcing shows that humidity of the residual layer can play an important role in the life-cycle of fog in more turbulent conditions when mixing between the fog layer and the residual layer is enhanced.

Conclusions

The processes dictating the evolution of a shallow stable radiation fog into a deep adiabatic radiation fog are not well understood, but are critical for improved prediction of fog. This work has used a set of single column model experiments to investigate the impact that humidity and wind-driven mixing in the residual layer can have on the development of shallow stable radiation fog, including the transition to a deep adiabatic radiation fog.

Using a series of perturbed wind forcing experiments, it has been shown that turbulence has an important role in modifying the vertical profiles of humidity and temperature. In slightly stronger wind speed conditions the modification to the vertical profile of humidity has the consequence of slowing the rate of the vertical development of the fog during the shallow stable phase, thus prolonging the observed shallow stable radiation fog phase, and eventually leading to an earlier dissipation time.

The humidity of the residual layer has an important role on the timing of the stability transition. However, it has a more significant role during modestly higher wind speed conditions due to additional mixing between the residual layer and the surface layer. This additional mixing modifies the surface layer moisture and resultant liquid water content altering the rate of development of the fog layer in its shallow stable phase, thus affecting the transition timing.

In summary, subtle changes to wind speed and consequently turbulence as well the humidity of the residual layer have a significant effect on the evolution of shallow stable radiation fog; in particular the timing of the transition to a deep adiabatic radiation fog. Therefore, in order to forecast a fog event accurately it is necessary to accurately predict wind speed and humidity within ~0.5ms^{-1} at 10m and 3% relative humidity as these can change the timing of the transition to a deep adiabatic radiation fog by 8 hours 15 minutes and 2 hours 40 minutes respectively. A possible mitigation of this sensitivity might be the use of ensemble forecasts using suitable wind and humidity perturbations to represent the uncertainty in a fog forecast. Also, as the perturbations used in this study are similar to the errors in the observations used in data assimilation, the study highlights the importance of accurate and representative observations for accurate fog forecasts.

Acknowledgements

We acknowledge use of the Monsoon2, a collaborative high performance computing facility supplied under the Joint Weather and Climate Research Programme, a strategic partnership between the Met Office and the Natural Environment Research Council. Ian Boutle and Micheal Whitall are acknowledged for their assistance with the SCM. D. K. E. Smith was supported by NERC grant NE/M010325/1.

References

Best MJ, Pryor M, Clark DB, Rooney GG, Essery R, Ménard CB, Edwards JM, Hendry MA, Porson A, Gedney N, and Others. 2011. The Joint UK Land Environment Simulator (JULES), model description-Part 1: energy and water fluxes. *Geoscienti*fic *Model Development*, **4**(3):677-699.

Boutle I, Price J, Kudzotsa I, Kokkola H, and Romakkaniemi S. 2017. Aerosol-fog interaction and the transition to well-mixed radiation fog, *Atmos. Chem. Phys. Discuss*., https://doi.org/10.5194/acp-2017-765, in review.

Clark PA, Harcourt SA, Macpherson B, Mathison CT, Cusack S, and Naylor M. 2008 Prediction of visibility and aerosol within the operational Met Office Unified Model. I: Model formulation and variational assimilation, *Quart. J. Roy. Meteor. Soc.*, **134**, 1801–1816.

Duynkerke P. 1999. Turbulence, Radiation and fog in Dutch Stable Boundary Layers. *Boundary-Layer Meteorology*, **90**(3):447-477.

Edwards J and Slingo A. 1996. Studies with a flexible new radiation code. i: Choosing a configuration for a large-scale model. *Quart. J. Roy. Meteor. Soc.*, **122**(531):689-719.

Guedalia D. and Bergot T. 1994. Numerical forecasting of radiation fog. part ii: A comparison of model simulation with several observed fog events. *Monthly Weather Review*, **122**(6):1231-1246.

Gultepe I, Tardif R, Michaelides SC, Cermak J, Bott A, Bendix J, Müller MD, Pagowski M, Hansen B, Ellrod G, Jacobs W, Toth G, and Cober SG. 2007. Fog Research: A Review of Past Achievements and Future Perspectives. *Pure and Applied Geophysics*, **164**(6-7):1121-1159.

Koschmeider H. 1924. Therie der horizontalen sichtweite. *Beitr. Phys. Freien Atmosph.* **12**: 33–53, 171–181.

Lock AP, Brown AR, Bush MR, Martin GM, and Smith RNB. 2000. A New Boundary Layer Mixing Scheme. Part I: Scheme Description and Single-Colum Model Tests. *Monthly Weather Review*, **128**(9):3187-3199.

Porson A, Price J, Lock A, and Clark P. 2011. Radiation Fog. Part II: Large-Eddy Simulations in Very Stable Conditions. *Boundary-Layer Meteorology*, **139**(2):193-224.

Price J. 2011. Radiation Fog. Part I: Observations of Stability and Drop Size Distributions. *Boundary-Layer Meteorology*, **139**(2):167-191.

Price J, Lane S, Boutle I, Smith D, Bergot T, Lac C, McGregor J, Kerr-Munslow A, Pickering M, and Clark R. 2018. LANFEX: a field and modelling study to improve our understanding and forecasting of radiation fog, *Bull. Amer. Meteor. Soc.,* accepted.

Roach W and Brown R. 1976. The physics of radiation fog: I - a field study. *Quart. J. Roy. Meteor. Soc.*, **102**(432):313-333.

Rodhe B. 1962. The effect of turbulence on fog formation. *Tellus*, **14**(1):49 - 86.

Smith R. 1990. A scheme for predicting layer clouds and their water content in a general circulation model. *Quart. J. Roy. Meteor. Soc.*, **116**(492):435-460.

Wilson DR and Ballard SP. 1999. A microphysically based precipitation scheme for the UK Meteorological Office Unified Model. *Quart. J. Roy. Meteor. Soc.*, **125**(557):1607-1636.

Table & Figure Captions

Figure 1. Schematic showing the structure of a typical radiation fog during its life-cycle from pre-fog to a deep adiabatic radiation fog. The red arrows represent the region of the largest emission of longwave radiation, the curved blue arrow represents turbulent mixing, U is the wind speed, T is the temperature and RH the relative humidity.

Figure 2. Operational mean sea level pressure analysis produced by the UK Met Office for 1800 UTC 24 November 2014.

Figure 3. Time-series of liquid water content from the control SCM experiment (shading). The black dots are the observed fog top height.

Table 1. Formation, stability transition and dissipation time for the IOP1 observations, control simulation and the wind perturbation sensitivity experiments.

Figure 4. Simulated profiles of liquid water content (LWC gkg^{-1}), potential temperature (θ K), total water content (q_{tot} gkg^{-1}) and relative humidity (RH %) in columns from left to right at a) 1800 UTC, b) 2100 UTC, c) 0000 UTC, d) 0300 UTC for the wind perturbation experiments.

Figure 5. Simulated profiles of TKE (m^2s^{-2}, left) and total moisture flux ($kgm^{-2}s^{-1}$, right) at 1800 UTC for the wind perturbation experiments.

Figure 6. Simulated profiles of liquid water content (LWC gkg^{-1}), potential temperature (θ K), total water content (q_{tot} gkg^{-1}) and relative humidity (RH %) in columns from left to right at a) 1000 UTC, b) 1200 UTC for the wind perturbation experiments.

Table 2. Formation, stability transition and dissipation time for the IOP1 relative humidity perturbation sensitivity experiments.

Figure 7. Simulated profiles of liquid water content (LWC gkg^{-1}), potential temperature (θ K), total water content (q_{tot} gkg^{-1}) and relative humidity (RH %) in columns from left to right at a) 2100 UTC, b) 0000 UTC for the relative humidity perturbation experiments with the control wind forcing.

Table 3. Formation, stability transition and dissipation time for the IOP1 relative humidity perturbation sensitivity experiments with +3ms^{-1} wind forcing.

Figure 8. Simulated profiles of liquid water content (LWC gkg^{-1}), potential temperature (θ K), total water content (q_{tot} gkg^{-1}) and relative humidity (RH %) in columns from left to right at a) 0300 UTC, b) 0700 UTC c) 1000 UTC for the relative humidity perturbation experiments with the +3ms^{-1} wind forcing.

Figures

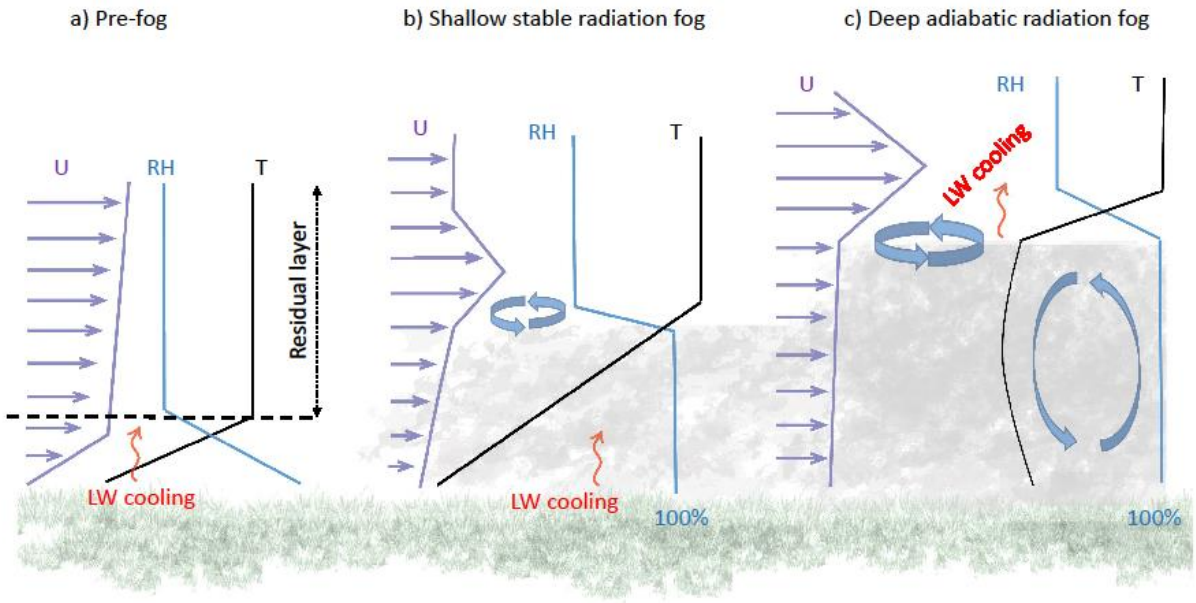

Figure 1.

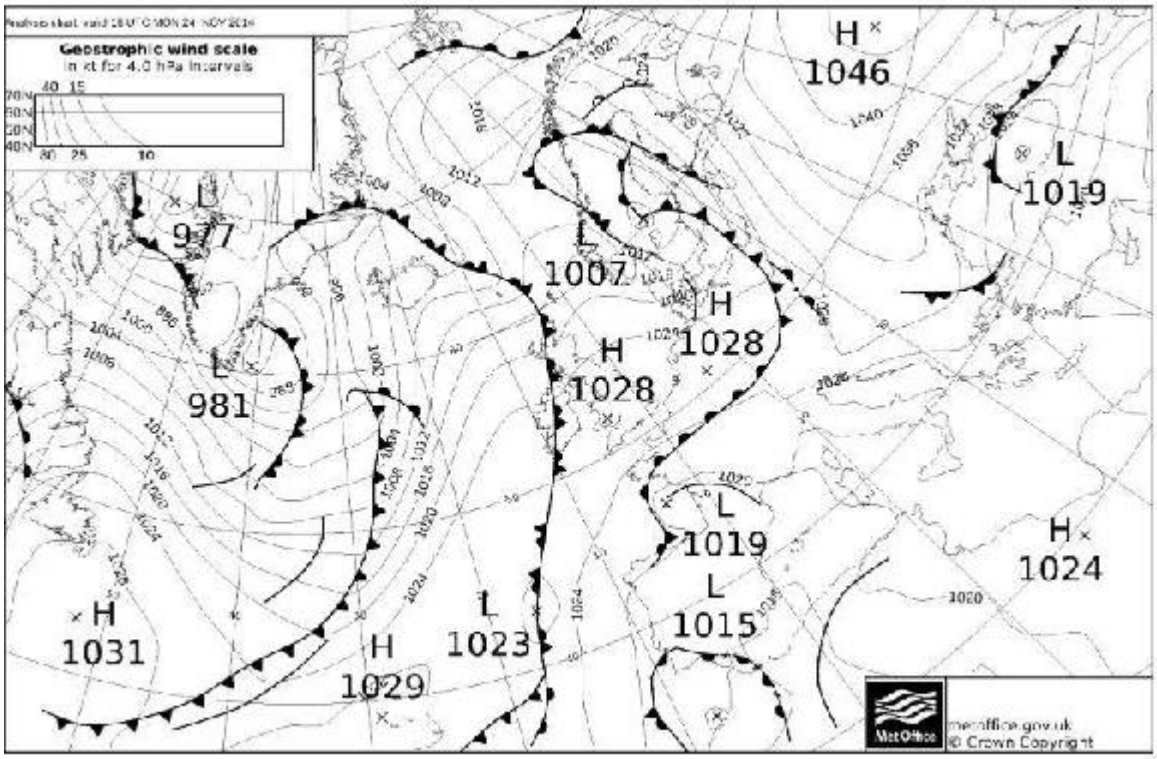
Geostrophic wind scale
in kt for 4.0 hPa intervals
40 15
80 25 10
H
1046
L
1019
L
977
L
1007
H
1028
H
1028
L
981
L
1019
H
1024
L
1015
H
1031
H
1029
L
1023
metoffice.gov.uk
© Crown Copyright

Figure 2.

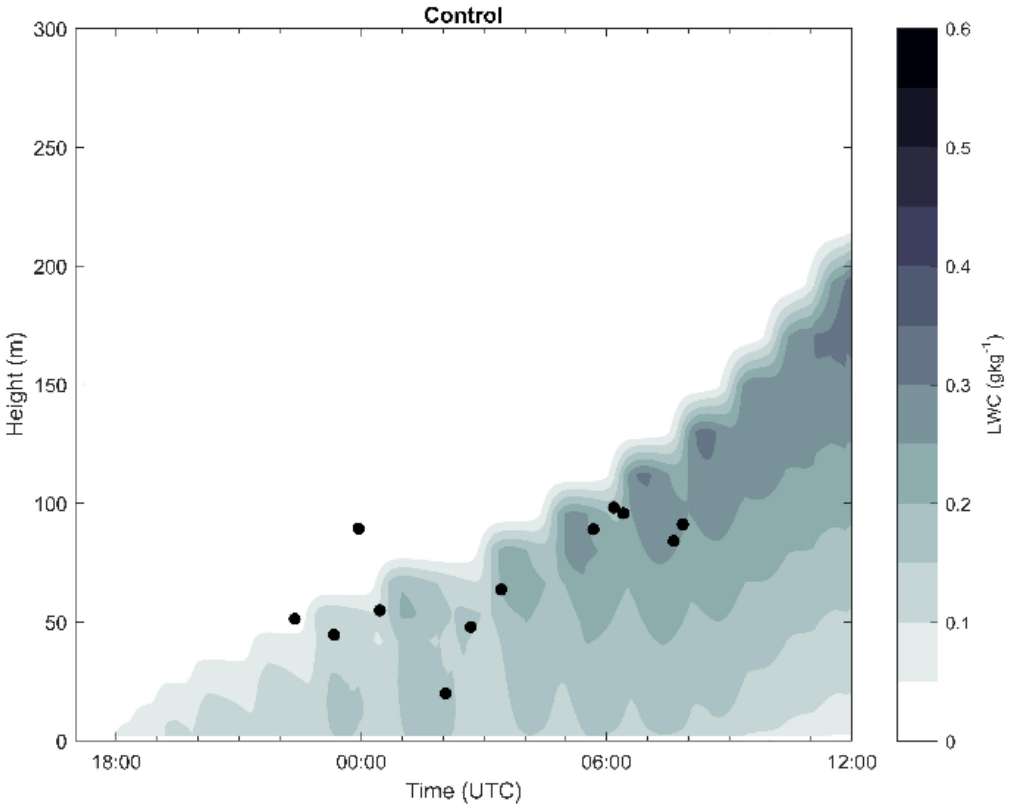

Figure 3.

Perturbation experiment	IOP1 – 24th/25th Nov 14		
	Formation	Stability transition	Dissipation
Observations	1750 UTC	0650 UTC	0815 UTC
Control	1750 UTC	2130 UTC	Persists to next day
+1ms^{-1} at 100m	1750 UTC	2300 UTC	Persists to next day
+2ms^{-1} at 100m	1750 UTC	0200 UTC	1200 UTC
+3ms^{-1} at 100m	1750 UTC	0545 UTC	1100 UTC

Table 1.

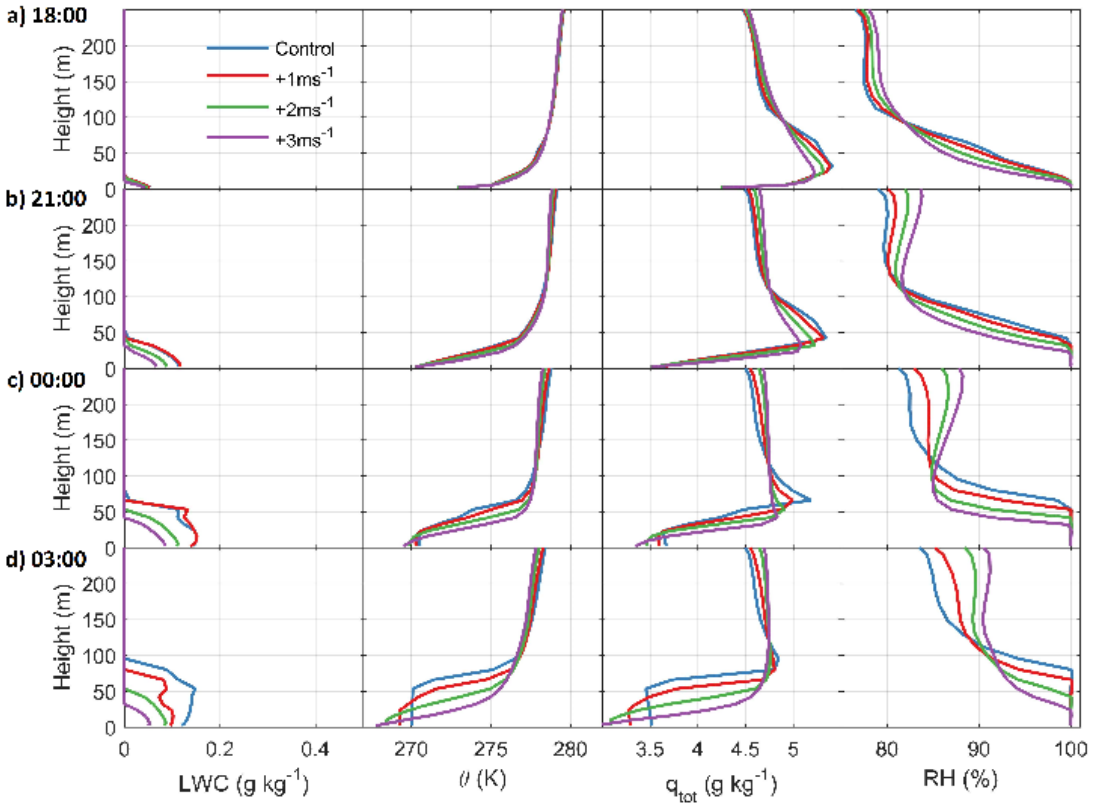
a) 18:00
b) 21:00
c) 00:00
d) 03:00
Control
+1ms-1
+2ms-1
+3ms-1
Height (m)
0
50
100
150
200
0
0.2
0.4
LWC (g kg-1)
270
275
280
θ (K)
3.5
4
4.5
5
qtot (g kg-1)
80
90
100
RH (%)

Figure 4.

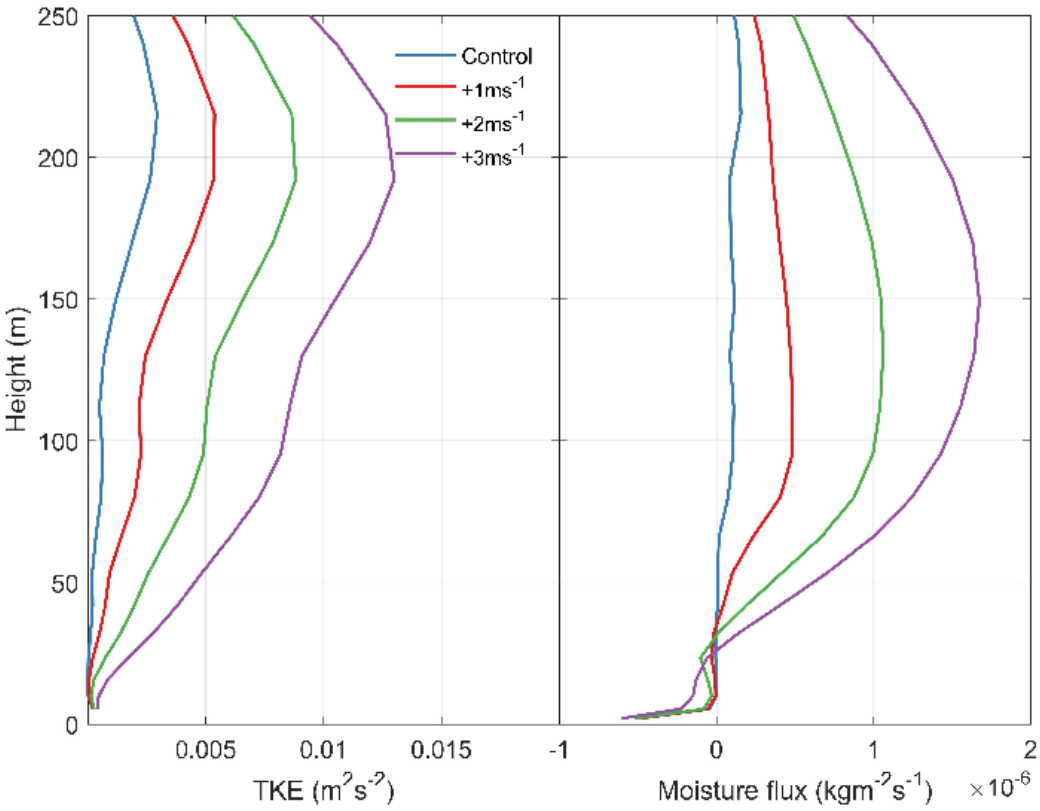
250
200
150
100
50
0
Height (m)
Control
+1ms-1
+2ms-1
+3ms-1
0.005
0.01
0.015
TKE (m2s-2)
-1
0
1
2
Moisture flux (kgm-2s-1)
×10-6

Figure 5.

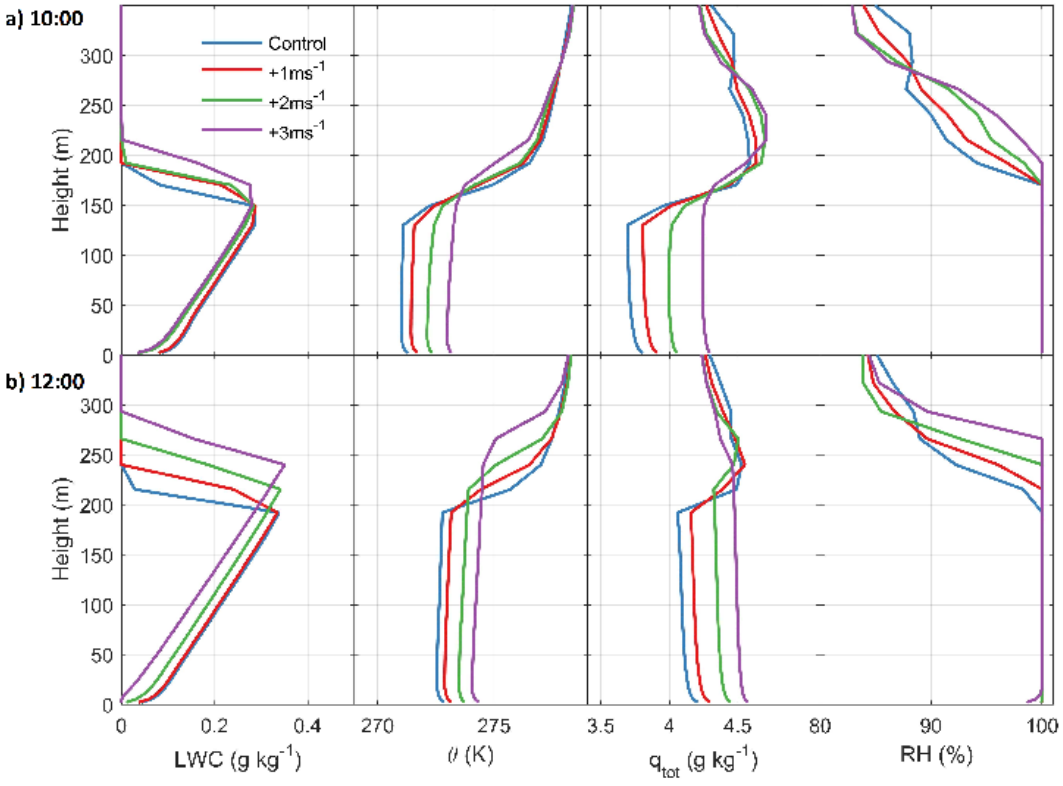

Figure 6.

Perturbation experiment	IOP1 – 24th/25th Nov 14		
	Formation	Stability transition	Dissipation
-3% RH	1750 UTC	2230 UTC	Persists to next day
Control	1750 UTC	2130 UTC	Persists to next day
+3% RH	1750 UTC	2100 UTC	Persists to next day

Table 2.

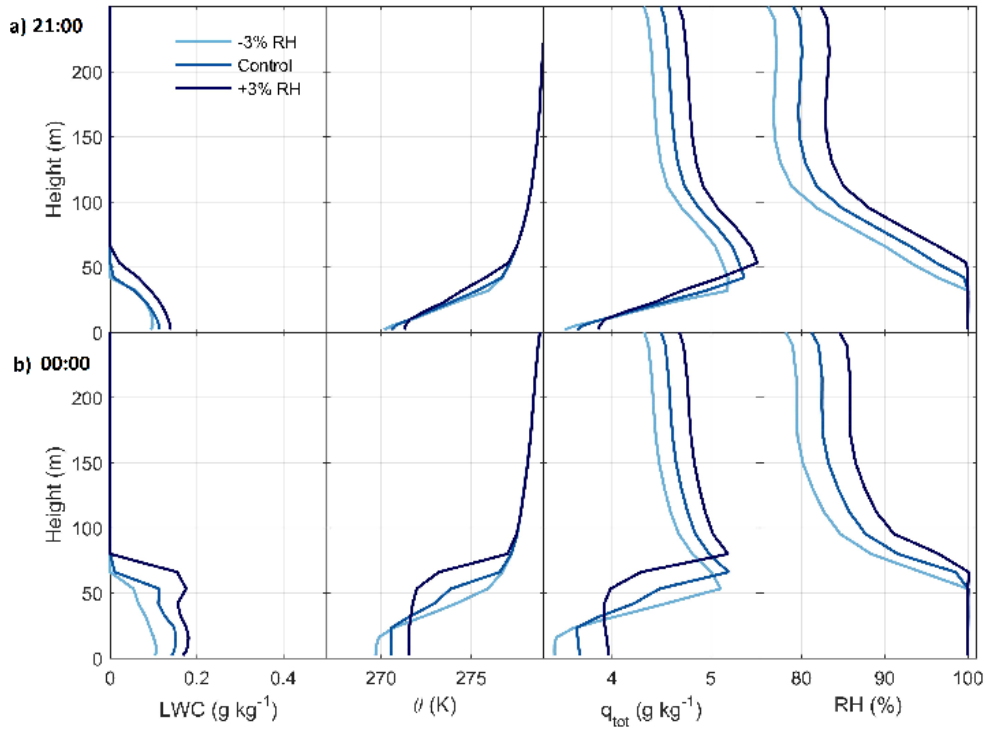

Figure 7.

Perturbation experiment	IOP1 – 24th/25th Nov 14		
	Formation	Stability transition	Dissipation
-3% RH and +3ms^{-1} at 100m	1750 UTC	0800 UTC – after sunrise	0930 UTC
+3ms^{-1} at 100m	1750 UTC	0545 UTC	1100 UTC
+3% RH and +3ms^{-1} at 100m	1750 UTC	0305 UTC	1130 UTC

Table 3.

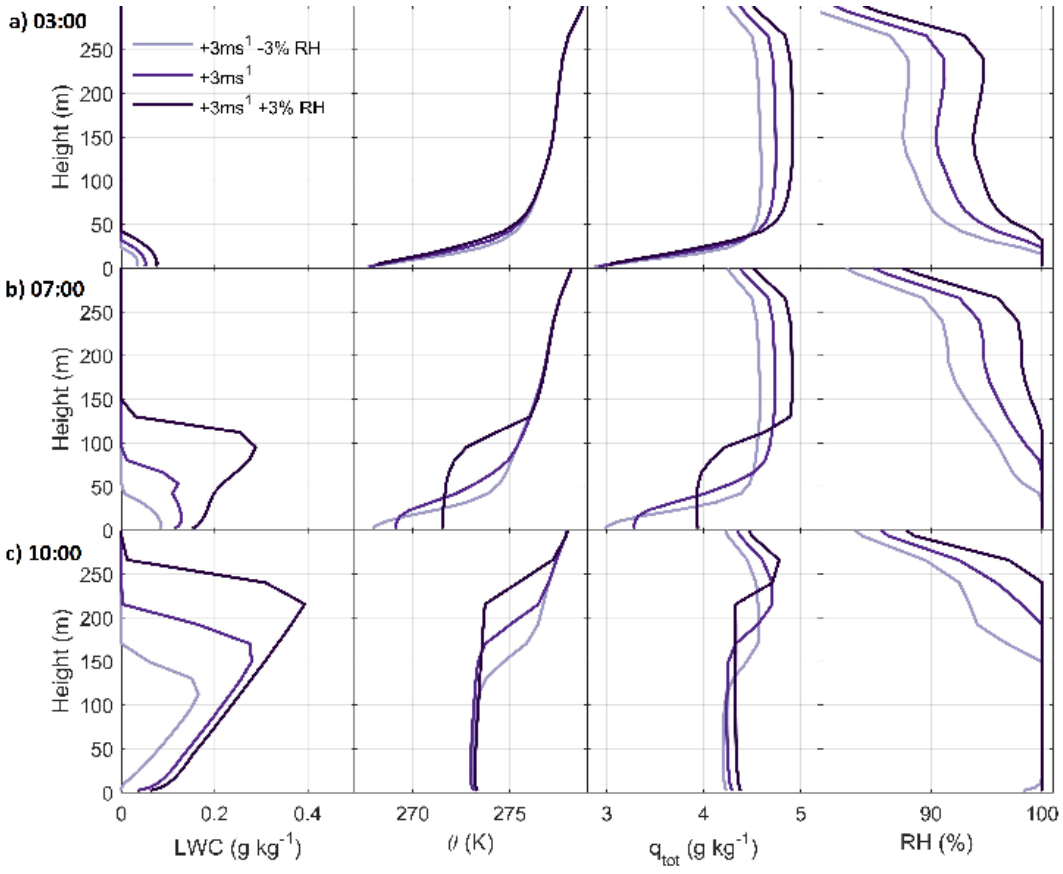
a) 03:00
b) 07:00
c) 10:00
+3ms^{1} -3% RH
+3ms^{1}
+3ms^{1} +3% RH
Height (m)
0
50
100
150
200
250
0
0.2
0.4
LWC (g kg^{-1})
270
275
θ (K)
3
4
5
q_{tot} (g kg^{-1})
90
100
RH (%)

Figure 8.